nature communications

Article

https://doi.org/10.1038/s41467-025-63844-x

Iron and oxygen vacancies co-modulated adsorption evolution and lattice oxygen dual-path mechanism for water oxidation

Received: 3 April 2025

Accepted: 1 September 2025

Published online: 02 October 2025

Check for updates

Xiwen Tao[1], Li Hou[1] ✉, Xinyi Wang[1], Jing Jin[1], Huana Li[1] & Faming Gao[1,2] ✉

Conjointly activating metal and oxygen sites to trigger the adsorbate evolution and lattice oxygen mechanisms coupled path holds promise for balancing activity and stability in oxygen evolution reaction catalysts, yet confronting great challenges. Herein, we develop Fe species and oxygen vacancies co-regulated Ni-(oxy)hydroxide from the deep reconstruction of Fe-Ni_2P/$NiMoO_4$ pre-catalyst achieving the adsorbate evolution and lattice oxygen dual-path mechanism. Experimental details and theoretical calculation analysis reveal the enhanced adsorbate evolution mechanism kinetics at the Ni sites via the co-regulation of Fe species and oxygen vacancies, while the Fe incorporation activates the O sites with preferable adsorption free energy for lattice oxygen mechanism intermediates. Benefiting from the dual-path mechanism, the activated catalyst affords an ampere-scale current density of 1.0 A cm^{-2} at low overpotentials of 274.5 ± 4.2 and 299.1 ± 2.8 mV in alkaline freshwater and seawater, respectively, and maintains seawater electrocatalysis for 500 h in the anion exchange membrane water electrolysis. This work demonstrates a strategy to trigger the coupled mechanism for efficient and stable electrocatalytic water splitting under harsh conditions.

Alkaline water electrolysis, as an efficient, clean, and environmentally benign technology for hydrogen production, holds immense development promises[1]. However, the anodic oxygen evolution reaction (OER) goes through slow reaction dynamics because of the complicated four-electron transfer procedure, severely impeding the overall water splitting (OWS) efficiency[2,3]. Particularly in the harsh and complex seawater environment, the presence of insoluble impurities and the chloride evolution reaction (ClER) pose great challenges to the OER kinetics and long-term durability of anode[4,5]. Therefore, designing high-activity and robust OER catalysts is imperative to achieve the industry-scale freshwater and seawater oxidation[6,7].

Reported researches have confirmed that the intrinsic OER performance of electrocatalysts possesses strong relevance to the reaction pathway of active sites[8]. Generally, the main pathways for alkaline OER are classified into two main types: adsorbate evolution and lattice oxygen mechanisms (AEM and LOM)[9]. For the AEM, the binding strength between the metal sites and oxygenated intermediates (*O, *OH, and *OOH) plays a significant role in catalytic activity, wherein the inherent linear-scaling relationship ($\Delta G_{OOH} = \Delta G_{OH} + 3.2 \pm 0.2$ eV) of the binding energies between *OH and *OOH limits the minimal overpotential of 370 mV vs. RHE for accelerating water oxidation[10–13]. In sharp contrast, the LOM achieves efficient O_2 release via the direct coupling of *O and oxygen ligands, circumventing the high barrier step of *OOH formation, thus requiring a lower theoretical overpotential[12]. Nevertheless, the dominant LOM pathway involves repeated refilling/release of lattice oxygen, leading to the unstable structure, and consequently abating the activity and durability of catalysts[14]. Undoubtedly, compared with the single-path OER catalysts, dual-path catalysts following the AEM-LOM coupled mechanism can obviate the scaling relationship to achieve high OER activity without diminishing the stability[15,16]. However, developing

[1]Hebei Key Laboratory of Applied Chemistry, State Key Laboratory of Metastable Materials Science and Technology, Yanshan University, Qinhuangdao, China. [2]College of Chemical Engineering and Materials Science, Tianjin University of Science and Technology, Tianjin, China. ✉e-mail: holy@ysu.edu.cn; fmgao@ysu.edu.cn

dual-path catalysts faces various challenges, as achieving the simultaneous electron transfer process at both metal sites and lattice oxygen within a single component or coordination environment depends on the optimal covalency of metal-oxygen (M-O) bonds[8].

Nanorod-like nickel molybdate hydrate ($NiMoO_4{\cdot}xH_2O$), a prospective pre-catalyst, undergoes a complete reconstruction accompanied by co-leaching of crystal water and MoO_4^{2-} ions under the alkaline OER conditions, resulting in the transformation to γ-NiOOH with a nanocrystal-amorphous feature[17,18]. Moreover, the $NiMoO_4{\cdot}xH_2O$ derived γ-NiOOH is considered as an ideal substitute for RuO_2 and IrO_2 benchmarked catalysts due to the satisfactory OER performance[19]. Many outstanding works have so far confirmed that the reasonable modification strategies, such as introducing exogenous heteroatoms or heterostructures[20–22], can activate the lattice oxygen of $NiMoO_4{\cdot}xH_2O$ catalyst systems for translating the mechanism from AEM to LOM, resulting in the derived NiOOH with enhanced OER activity. On the other hand, introducing additional defects is a promising strategy to accelerate the reconfiguration of $NiMoO_4{\cdot}xH_2O$ and reduce the covalency of Ni-O bonds, which can effectively optimize the AEM mechanism of the active phase[23,24]. Thus, constructing the heteroatoms/oxygen vacancies co-regulated γ-NiOOH may potentially obtain the optimal M-O covalency, thereby simultaneously activating the metal sites and lattice oxygen.

In this work, the $NiMoO_4{\cdot}xH_2O$ serves as the pre-catalyst, while Fe-doped Ni_2P nanoparticles derived from the Prussian blue analog (NiFe-PBA) are introduced to optimize the electron configuration of Ni sites in $NiMoO_4$, thereby accelerating the deep reconstruction into the Fe atoms/oxygen vacancies co-modified γ-NiOOH active phase (O_V-Ni(Fe)OOH) during the electrochemical activation. A series of characterizations, including in-situ ^{18}O isotope-labeling differential electrochemical mass spectrometry (DEMS), in-situ surface-enhanced infrared absorption spectroscopy with attenuated total reflection (ATR-SEIRAS), and chemical probes, are employed to confirm the compatible pathway of AEM and LOM in the activated catalyst. Furthermore, the experimental details and density functional theory (DFT) analysis unveil that Fe dopants significantly increase the lattice oxygen activity, while the proper concentration of O_V regulates the Ni-O covalency and optimize the AEM kinetics. Benefiting from the AEM-LOM coupled mechanism and the notable mass transfer ability, the reconstructed OER catalyst in alkaline freshwater and seawater delivers the 1.0 A cm^{-2} current density at 274.5 ± 4.2 and 299.1 ± 2.8 mV, respectively. Moreover, the anion exchange membrane (AEM) seawater electrolyzer system assembled with Fe-Ni_2P/$NiMoO_4$ and $MoNi_4$ exhibits preeminent durability in the successive ampere-level seawater electrolysis for 500 h.

Results

Design and structural characterizations of pre-catalysts

Nanorod-like Fe-Ni_2P/$NiMoO_4$ arrays, as the pre-catalysts, were directly grown on the nickel foam (NF) via hydrothermal, ion-exchange, and low-temperature phosphating methods, as illustrated in Fig. 1a and Supplementary Fig. 1. The composition and crystal structure of the products during the synthesis process were identified via X-ray diffraction (XRD). In Fig. 1b and Supplementary Fig. 2, the characteristic peaks ascribing to $NiMoO_4{\cdot}xH_2O$ (PDF#024-7435) constantly persist in the diffraction patterns of $NiMoO_4$, PBA@$NiMoO_4$, and Fe-Ni_2P/$NiMoO_4$, indicating that the $NiMoO_4{\cdot}xH_2O$ phase is well-preserved. Significantly, the characteristic peaks of NiFe-PBA ($K_2FeNi(CN)_6$, PDF#023-0491) completely vanish after the low-temperature phosphating, while the new peaks emerge at 41.1, 43.5, 47.7, and 53.7° that can be indexed to Ni_2P (PDF#074-1385) in Fe-Ni_2P/$NiMoO_4$. Due to the absence of angle shift, Fe atoms are present in the Ni_2P lattice as substitutional dopants, rather than interstitial dopants. The scanning electron microscope (SEM) was manipulated to observe the geometry morphology of samples. The arrays composed of $NiMoO_4{\cdot}xH_2O$ nanorods possessing an average size of 716 nm and smooth surface are evenly grown on the NF framework (Supplementary Fig. 3). Following the ion-exchange process, NiFe-PBA nanocubes cover the surface of nanorods, forming a distinctive top-hollow structure (Supplementary Fig. 4). As depicted in Fig. 1c, d and Supplementary Fig. 5, the array and top-hollow configuration are retained, while the PBA nanocubes melt and coalesce to form a continuous shell layer encapsulating the nanorods, with dimensions ranging around 900–950 nm. This morphology is advantageous for accelerating reaction kinetics and enhancing mass transfer. Notably, we found that the dosage of $C_6H_5Na_3O_7$ and $NaH_2PO_2{\cdot}H_2O$ are identified as crucial factors in the synthesis and morphology control of the electrocatalysts (Supplementary Figs. 6–8). Experimental results demonstrate that the absence of $C_6H_5Na_3O_7$ is detrimental to the growth of NiFe-PBA on the surface of $NiMoO_4{\cdot}xH_2O$. Conversely, increasing the amount of $C_6H_5Na_3O_7$ from 1.2 to 2.4 mmol gives rise to the disappearance of the top-hollow configuration in the as-synthesized materials. Similarly, the phosphating process of NiFe-PBA is incomplete when the amount of $NaH_2PO_2{\cdot}H_2O$ is 0.9 g. However, increasing the dosage of phosphorus source to 2.7 g also results in the loss of the top-hollow structure.

Transmission electron microscopy (TEM) and high-resolution TEM (HRTEM) were employed to investigate the detailed geometric and phase structures of Fe-Ni_2P/$NiMoO_4$ composite. In Fig. 1e, the hierarchical nanorod structure composed of PBA derivative and $NiMoO_4{\cdot}xH_2O$ is in good accordance with the SEM images. HRTEM image obtained from the exposed interior of the nanorod reveals an interplanar parameter of 0.214 nm, which can be indexed to the (111) facet for Ni_2P. The above observation aligns with the results of the XRD pattern. We employed the focused ion beam (FIB) treatment to expose the cross-section of the Fe-Ni_2P/$NiMoO_4$ composite, and the corresponding TEM and HRTEM images are presented in Fig. 1f, Supplementary Figs. 9 and 10. The hierarchical configuration, comprising the amorphous layer, Fe-Ni_2P nanoparticles, and $NiMoO_4{\cdot}xH_2O$ core, can be distinctly visualized. Furthermore, the magnified high-angle annular dark-field scanning transmission electron microscopy (HAADF-STEM) image, which corresponds to the region of $NiMoO_4{\cdot}xH_2O$ core (Fig. 1g). Two labeled crystal lattices with measured interplanar distances of 0.284 and 0.306 nm are identified, which correspond to the (02-1) and (20-1) planes of $NiMoO_4{\cdot}xH_2O$, respectively (Supplementary Fig. 11). Based on the angular and lattice spacing relationships intrinsic to the anorthic system, the theoretical angle between the [02-1] and [20-1] crystal orientations is calculated to be 91°, which aligns well with the measured value (as illustrated in the inset of Fig. 1g). The high crystallinity of $NiMoO_4{\cdot}xH_2O$ within the composite is collectively confirmed via above results. Energy-dispersive X-ray spectroscopy (EDS) surface and line scans confirm that the Mo element is exclusively found in the core region, while Fe and P elements are predominantly present on the shell (Supplementary Figs. 12 and 13). Notably, as shown in Fig. 1h–m, the larger mapping area of the Ni element (compared to Mo element) in the cross-section of the composite demonstrates the tight binding between Fe-Ni_2P and $NiMoO_4{\cdot}xH_2O$, which is conducive to electron transfer between the two phases, thereby optimizing the electron configuration of Ni sites and accelerating the reconstruction process. In addition, the accurate element contents were substantiated by the inductively coupled plasma-mass spectrometry (ICP-MS), which shows that the contents of Fe and Ni in Fe-Ni_2P/$NiMoO_4$ is 7.96 and 34.97 at.%, respectively (Supplementary Table 1).

To elucidate the role of each individual component within the composite catalyst system, we synthesized the Fe-doped Ni_2P (marked as Fe-Ni_2P) derived from NiFe-PBA on the NF using the same methods. The XRD patterns, SEM images, and EDS mapping are presented in Supplementary Figs. 14–16. The electronic structures of Fe-Ni_2P/$NiMoO_4$, Fe-Ni_2P, and $NiMoO_4$ were analyzed by X-ray photoelectron spectroscopy (XPS) (Supplementary Fig. 17). For the high-resolution Ni 2*p* spectrum of Fe-Ni_2P/$NiMoO_4$ composite (Supplementary Fig. 17b),

https://doi.org/10.1038/s41467-025-63844-x

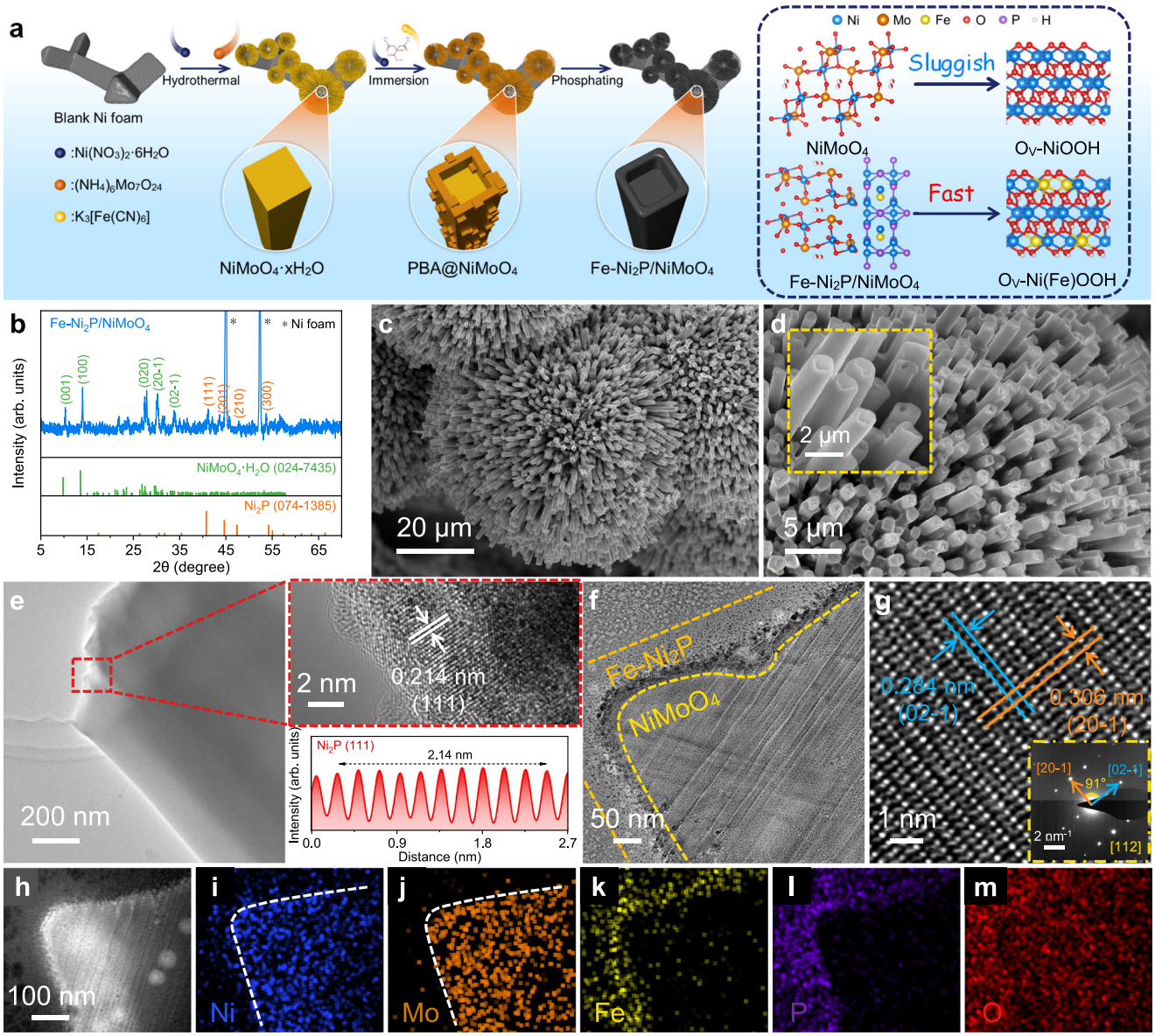

Fig. 1 | Preparation scheme, and structural characterizations of the Fe-Ni_2P/$NiMoO_4$ pre-catalyst. a Diagrammatic sketch presenting the fabrication procedure of the Fe-Ni_2P/$NiMoO_4$ composite, and the electrochemical reconstruction product. **b** XRD pattern for Fe-Ni_2P/$NiMoO_4$. **c** SEM image. **d** Enlarged SEM image. **e** TEM, HRTEM images, and the corresponding intensity-distance images for the lattice fringe. **f** The cross-sectional TEM image of Fe-Ni_2P/$NiMoO_4$. **g** The magnified HAAD-STEM image in the region of $NiMoO_4$ (inset: SAED pattern). **h** The cross-sectional HAAD-STEM image, and (**i**–**m**) corresponding EDS element mapping images. Source data are provided as a Source Data file.

the deconvoluted peaks at 856.2 and 874.0 eV corresponding to Ni^{2+} species exhibit a negative shift in comparison with pure Fe-Ni_2P and a positive shift compared to pristine $NiMoO_4$. The Fe 2*p* spectra in Fe-Ni_2P/$NiMoO_4$ and Fe-Ni_2P reveal the characteristic signal of Fe^{2+} and Fe^{3+}. Specifically, the significant positive shift in the bonding energy of the Fe^{3+} peaks indicates that the Fe species in Fe-Ni_2P/$NiMoO_4$ composite possess a higher oxidation state in contrast to that of Fe-Ni_2P. These results reveal that the interaction between Fe-Ni_2P and $NiMoO_4$ modulates the electronic structure of Ni in $NiMoO_4$, concomitantly enhances the overall oxidation state of Fe sites, thereby increasing the conductivity and accelerating the deep reconfiguration process of the pre-catalyst. The depth-profile XPS spectra (Supplementary Fig. 18) illustrate that the signal associated with the Ni-P peaks evolves with the increasing etch level. This observation unveils that Fe-Ni_2P predominantly concentrated within the interior of the nanorods, which agrees well with the cross-sectional TEM results.

Electrochemical activation of active phases

As presented in Supplementary Figs. 20–22, the optimization processes of current density and potential in the cyclic voltammetry (CV), linear sweep voltammetry (LSV) and chronopotentiometry (CP) measurements, respectively, reveal the dynamic reconstruction and active phases generation of the pre-catalysts for pristine $NiMoO_4$ and Fe-Ni_2P/$NiMoO_4$. It is apparent that the Fe-Ni_2P/$NiMoO_4$ electrocatalyst exhibits faster reconfiguration kinetics and a more pronounced accumulation of the γ-NiOOH active phase, resulting from enhanced charge transfer capability by reason of the modification of Fe-Ni_2P species. To explore the dynamic reconstruction of pre-catalysts in OER conditions, in situ electrochemical and spectroscopic characterizations were employed. Firstly, we used the in-situ electrochemical impedance spectroscopy (in-situ EIS) to study the OER kinetics and electrocatalyst/electrolyte interface. The low-frequency region (10^{-2} – 10^{1} Hz) of the impedance spectra corresponds to charge transfer between

active species and OER intermediates, while the high-frequency region ($10^1 - 10^4$ Hz) reflects electron transfer procedures of the catalyst inner during the electrooxidation reaction[25]. As displayed in the Bode plots (Supplementary Fig. 23), the phase angle (θ) in the high-frequency region gradually decreases with the increasing applied potentials, wherein the Fe-Ni_2P/$NiMoO_4$ possesses the smallest switched potential at 1.38 V vs. RHE, lower than that of $NiMoO_4$ (1.41 V vs. RHE) and Fe-Ni_2P (1.41 V vs. RHE), indicating that the interaction between Fe-Ni_2P and $NiMoO_4$ accelerates the generation of the active phase. Then, the phase-evolution process of pre-catalysts was identified by in-situ Raman spectra with controlled applied potentials (Fig. 2a and Supplementary Fig. 24). As the progressing of the electro-oxidation process, the characteristic bonds of Mo-O and Mo = O vibrations at 347, 825, 875, and 950 cm^{-1} gradually diminish and eventually disappear, ascribing to MoO_4^{2-} leaching under OER conditions. Especially, the typical active species of γ-NiOOH can be confirmed by the presence of two characteristic peaks at 472 and 552 cm^{-1} corresponding to E_g and A_{1g} vibration modes for Ni^{3+}-O, respectively[26]. Significantly, the conversion of Fe-Ni_2P/$NiMoO_4$ to γ-NiOOH occurs at a lower potential (1.40 V), further demonstrating a faster electrochemical reconstruction.

Following the electrochemical activation process, we obtained the reconstructed catalysts (labeled as R-*). We then further analyzed their crystalline, geometric, and electronic structures to elucidate the underlying mechanisms contributing to the AEM-LOM dual-path. The XRD pattern of R-Fe-Ni_2P/$NiMoO_4$ (Supplementary Fig. 25) manifests that the characteristic peaks of $NiMoO_4{\cdot}xH_2O$ completely disappear, being replaced by two new peaks located at 35.0 and 61.1°, which can be indexed to the (101) and (310) facets of NiOOH (PDF#027-0956). This transformation is also observed in the XRD pattern of R-$NiMoO_4$. Besides, three weak peaks located at 41.1, 47.8, and 54.6° in R-Fe-Ni_2P/$NiMoO_4$ are attributed to residual Ni_2P species, which maintain the high conductivity of the whole catalyst. In Ni-(oxy)hydroxides, the ratio for bending and stretching vibration modes intensity (I_B/I_S) can function as an indicator of disorder level, in which the lower I_B/I_S value represents a higher disorder structure[27]. As profiled in Supplementary Fig. 26, the I_B/I_S value for R-Fe-Ni_2P/$NiMoO_4$ is measured at 1.37, which contrasts sharply with the 2.16 value found in R-$NiMoO_4$, indicating that Fe species from Fe-Ni_2P migrate into the lattice of restructured NiOOH during electrochemical activation, resulting in a lower crystallinity structure.

SEM (Fig. 2b, c) and TEM (Supplementary Fig. 27) images reveal that the morphology of nanorod arrays is preserved in the reconstructed electrocatalyst, but the individual nanorods have evolved into a loose and porous structure. As shown in the HRTEM images (Fig. 2d, e), the interplanar distance of 0.249 nm corresponds to the (101) facet of γ-NiOOH, aligning to the XRD results. Notably, discontinuous lattice fringes are present in the material (the yellow circle highlight in Fig. 2e), ascribing to the defects via the incorporation of O_V. The EDS surface and line scans, as presented in Fig. 2f–k and Supplementary Fig. 28, demonstrate a uniform distribution of the Fe element throughout the entire nanorod, rather than a concentration in the shell, indicating the introduction of Fe dopants into the whole active phase. Whilst the marked decrease in the mapping intensity of Mo and P elements, as observed, originates from the leaching of MoO_4^{2-} and P species under OER conditions. As shown in Supplementary Table 1, the ICP-MS results further reveal the content of Fe is determined to be 13.32 at% as the modifier, along with the massive dissolution of Mo and P elements. These results confirm that O_V-Ni(Fe)OOH is the real active species in R-Fe-Ni_2P/$NiMoO_4$.

XPS analysis is applied to explore the surface oxidation state changes between pre- and post-catalysts, as well as the differences in the electronic environment between reconstructed products. As illustrated in Supplementary Fig. 29, the proportion of Ni^{3+} and Fe^{3+} of R-Fe-Ni_2P/$NiMoO_4$ exhibits a notable increase compared to the initial Fe-Ni_2P/$NiMoO_4$. Meanwhile, the XPS signals related to the Mo element and Ni-P bond almost disappear. These results are consistent with XRD, Raman spectroscopy, EDS mapping, and ICP-MS, further confirming the efficient and deep transformation during the electrochemical activation. It is noteworthy that the proportion of O_V in the O 1*s* spectrum slightly increases from 28.08% to 30.98% after reconstruction (Supplementary Table 2). The electron paramagnetic resonance (EPR) spectra (Supplementary Fig. 30a) also provide evidence of the appropriate increase in O_V, which is conducive to optimizing the AEM kinetics. In the Ni 2*p* spectrum (Fig. 2l), we found that the signal peaks of Ni $2p_{3/2}$ orbital for R-Fe-Ni_2P/$NiMoO_4$ are centered between those of R-Fe-Ni_2P and R-$NiMoO_4$, illustrating that Fe dopants and O_V primarily act as electron acceptors and donors, respectively, and co-modulate the electronic structure of NiOOH. Meanwhile, as presented in Fig. 2m, the peaks of lattice oxygen (M-O) for R-Fe-Ni_2P/$NiMoO_4$ and R-Fe-Ni_2P significantly shift toward the higher binding energy relative to that of R-$NiMoO_4$, unveiling the enhanced Ni-O covalent bonds and lattice oxygen activity following the introduction of Fe species[28]. Moreover, the slight increasing of O_V has been also detected in the XPS and EPR spectra of R-$NiMoO_4$ (Fig. 2m and Supplementary Fig. 30c), indicating that co-leaching of MoO_4^{2-} and crystalline water is the primary reason for the generation of O_V in the $NiMoO_4$ system[29]. The binding energy of Fe 2*p* peak for R-Fe-Ni_2P/$NiMoO_4$ exhibits a significant negative shift with respect to that of R-Fe-Ni_2P (Fig. 2n), which indicates that the over-oxidation of Fe species in active phases has been suppressed, which is favorable to circumvent the Fe leaching[30]. The absence of P and Mo element signals is also observed in Supplementary Fig. 31 for XPS spectra of R-Fe-Ni_2P and R-$NiMoO_4$, respectively.

Electrocatalytic OER performance

We assembled a typical three-electrode system, directly employing the pre-catalysts or benchmarks as the work electrode to test their electrocatalytic performance in O_2-saturated 1 M KOH. The activated Fe-Ni_2P/$NiMoO_4$ catalyst exhibits the optimal OER performance (as seen in Fig. 3a and Supplementary Fig. 32), delivering current densities of 10, 100, 500, and 1000 mA cm^{-2} at 197, 221, 251, and 275 mV, respectively, which is in excess of other counterparts. Fe-Ni_2P/$NiMoO_4$ exerts the lowest Tafel slope (30.51 mV dec^{-1}), as described in Supplementary Fig. 33, suggesting the superior OER reaction kinetics. Simultaneously, Fe-Ni_2P/$NiMoO_4$ also presents the accelerated charge-transfer capacity, featuring the optimal charge transfer resistance (R_{ct}) of 0.77 Ω, lower than that of Fe-Ni_2P (2.91 Ω), $NiMoO_4$ (1.55 Ω), and RuO_2 (12.61 Ω) in Supplementary Fig. 34 and Table 3. Moreover, the electrochemical surface area (ECSA) and turnover frequency (TOF) were calculated to assess the intrinsic OER activity (Supplementary Figs. 35 and 36). Apparently, Fe-Ni_2P/$NiMoO_4$ exhibits the highest ECSA-normalized current density and TOF value. In summary, the systematic comparison of OER activity, Tafel slope, R_{ct}, C_{dl}, and TOF is presented in Fig. 3b, and Fe-Ni_2P/$NiMoO_4$ exhibits superior overall OER performance compared to all control samples. Compared with recently reported OER catalysts (Supplementary Table 4), Fe-Ni_2P/$NiMoO_4$ demonstrates the immense prospect for application, especially under ampere-level current densities.

Following that, we measured the OER efficiency of catalysts in 1 M KOH + 0.5 M NaCl and 1 M KOH + seawater solution. In Fig. 3c, d and Supplementary Fig. 37, Fe-Ni_2P/$NiMoO_4$ exhibits low overpotentials of 296 and 299 mV at 1000 mA cm^{-2} current density in alkaline artificial and natural seawater, respectively, accompanied by low Tafel slopes (36.14 and 39.64 mV dec^{-1}). The performance of Fe-Ni_2P/$NiMoO_4$ outperforms that of control samples and the state-of-the-art catalysts (Supplementary Table 5), further demonstrating its underlying application value. Notably, the R_{ct} of $NiMoO_4$ discernibly increases from 3.21 to 7.89 Ω when the electrolyte is switched from simulated seawater to real seawater, whereas Fe-Ni_2P/$NiMoO_4$ and Fe-Ni_2P exhibit

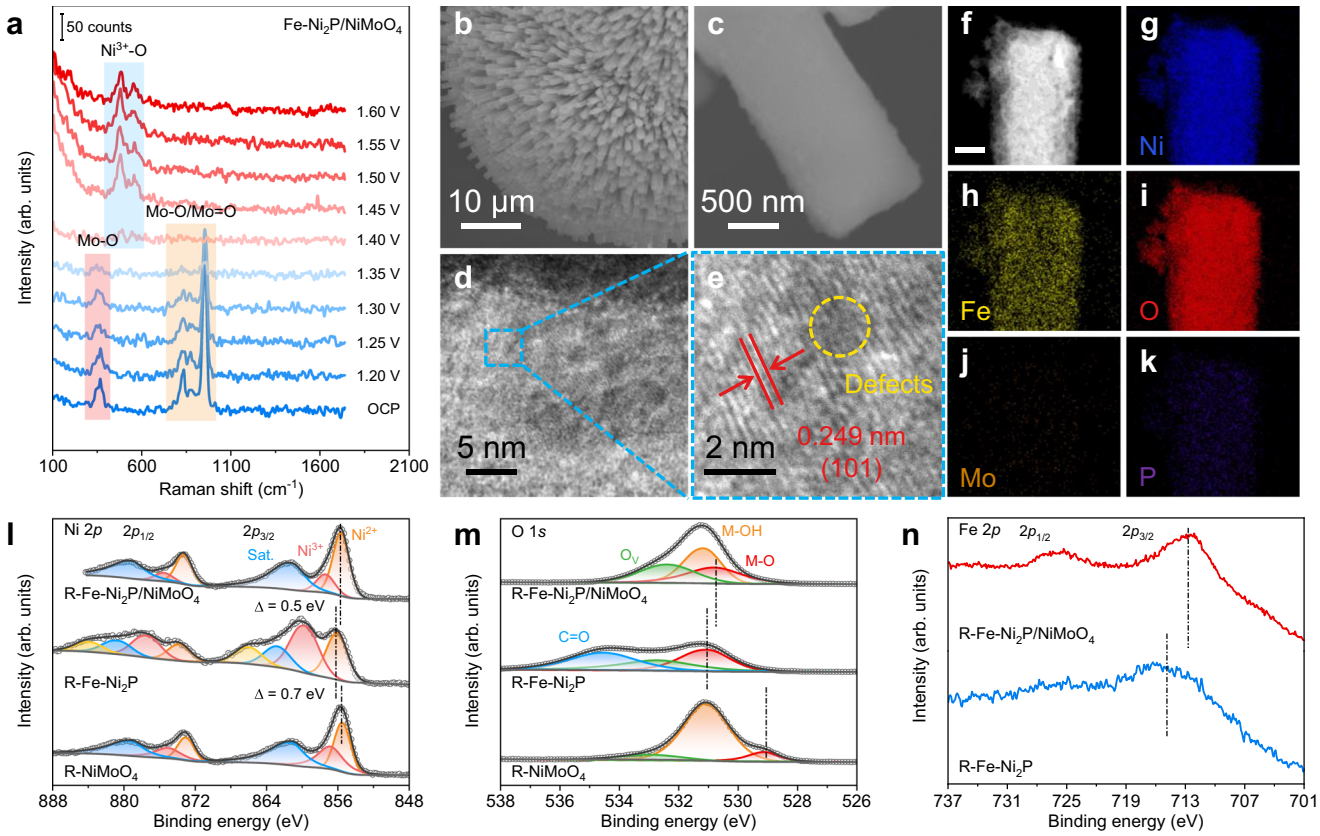

Fig. 2 | Electrochemical activation and structural characterizations of activated catalysts. a In situ Raman spectroscopy analysis of catalyst reconstruction for Fe-Ni_2P/$NiMoO_4$. The geometric structure of the activated catalyst for R-Fe-Ni_2P/$NiMoO_4$. **b** SEM, (**c**)enlarged SEM, (**d**) HRTEM, and (**e**) enlarged HRTEM images. **f** The HAAD-STEM image of R-Fe-Ni_2P/$NiMoO_4$ (scale bar: 100 nm), and (**g**–**k**) corresponding EDS element mapping images. The electronic structure of activated catalysts. **l** Ni 2*p*, (**m**) O 1*s*, and (**n**) Fe 2*p* high-resolution XPS spectra. Source data are provided as a Source Data file.

slight degradation (Fig. 3e and Supplementary Tables 6 and 7). Meanwhile, as illustrated in the Tafel corrosion plots and derived corrosion data (Fig. 3f and Supplementary Table 8), the Fe-Ni_2P/$NiMoO_4$ electrode possesses higher corrosion potential at − 0.214 V vs. SCE, accompanied by a lower current density of 0.124 mA cm^{-2} compared with Fe-Ni_2P and initial $NiMoO_4$. These results reveal that the outstanding performance of Fe-Ni_2P/$NiMoO_4$ in the alkaline seawater solution is attributed to the high intrinsic activity and the presence of an amorphous protective layer, which effectively prevents the ClER and mitigates the impact of impurities[31,32].

Fe-Ni_2P/$NiMoO_4$ exhibits notable long-term durability at 1.0 A cm^{-2} for 1000 h in alkaline freshwater with negligible attenuation (Fig. 3g). In contrast, a significant potential decay was observed for Fe-Ni_2P (Supplementary Fig. 38). Combined with the reduced concentration of Fe and Ni species in the electrolyte of Fe-Ni_2P/$NiMoO_4$ compared to Fe-Ni_2P (Supplementary Fig. 39), it is confirmed that the AEM-LOM dual-path efficiently suppresses the segregation of metal sites caused by lattice oxygen loss, thereby preventing further degradation of stability. Furthermore, the Fe-Ni_2P/$NiMoO_4$ exhibits superior mechanical stability (Supplementary Fig. 40) as well as enhanced hydrophilicity/aerophobicity properties (Supplementary Fig. 41), which effectively prevent the structural collapse induced by O_2 bubble shock under ampere-level current densities. In addition, the stability of Fe-Ni_2P/$NiMoO_4$ was further evaluated at 1.0 A cm^{-2} for 500 h in both alkaline artificial and natural seawater. The residual chlorine detection (Supplementary Fig. 42) demonstrates that no ClO^- was generated during the seawater oxidation process. The absence of ClER leads to a commendable Faraday efficiency of 98.41 ± 0.67% in alkaline seawater, which is remarkably close to the results obtained in alkaline freshwater (98.84 ± 0.62%) (Supplementary Figs. 43–45).

AEM-LOM dual-path OER mechanism analysis

We further explore the activation conditions of the dual-path OER mechanism involved in Fe-Ni_2P/$NiMoO_4$. As profiled in Supplementary Fig. 46, the OER activity under different pH values was used to preliminarily determine the pathway of the activated electrocatalysts. Generally, a close association exists between the pH dependence and the proton-reaction order (ρ), with a ρ value close to 1 manifesting a non-concerted proton-electron transfer pathway[33]. Therefore, Fe-Ni_2P/$NiMoO_4$, $NiMoO_4$, and Fe-Ni_2P catalysts may undergo the LOM pathway (Fig. 4a). Notably, the strongest pH-dependence of Fe-Ni_2P/$NiMoO_4$ at 1.55 V vs. RHE suggests that it possesses higher lattice oxygen activity. Furthermore, the O_2 signals released by the ^{18}O isotope-labeled Fe-Ni_2P/$NiMoO_4$ during the OER process in $H_2{}^{16}O$ were captured by in-situ DEMS to analyze the OER mechanism (Supplementary Fig. 47). As shown in Fig. 4b, the mass spectrometer detected distinct signals of $^{16}O^{16}O$ and $^{16}O^{18}O$ gas, corresponding to the O_2 products from AEM and LOM pathways, respectively[34]. Meanwhile, the absence of a significant $^{18}O^{18}O$ signal suggests that only one lattice oxygen participates in the reaction. In addition, in-situ ATR-SEIRAS was employed to investigate the interaction between oxygen-containing intermediates and the catalytic surface during the OER process (Supplementary Fig. 48). In Fig. 4c, two distinct peaks are observed in the range from 1000 to 1100 cm^{-1}, which emerged as the applied anodic potentials increased. The peak centered at 1029 cm^{-1} can be assigned to the *OOH intermediate generated via the AEM pathway, while the accompanying peak located at 1065 cm^{-1} arises from the interaction

https://doi.org/10.1038/s41467-025-63844-x

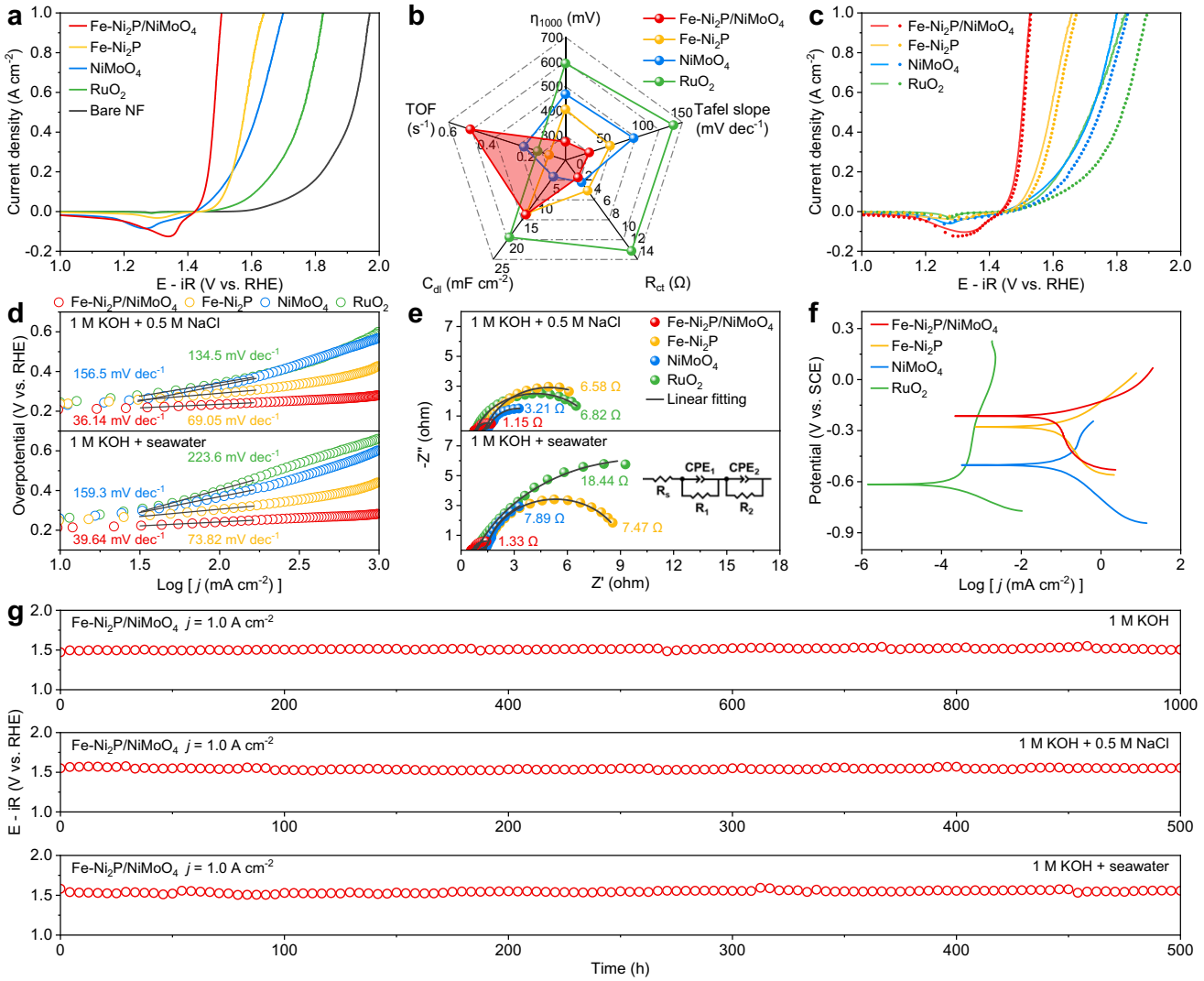

Fig. 3 | The electrocatalytic performance of as-prepared electrocatalysts. a OER LSV curves in 1 M KOH solution with 90% iR compensation. **b** Comprehensive comparisons for OER performance, Tafel slopes, R_{ct}, C_{dl}, and TOF of Fe-Ni_2P/$NiMoO_4$ with other samples in 1 M KOH. **c** OER LSV curves in alkaline brackish water (solid) and alkaline real seawater (dot), and (**d**) corresponding Tafel slopes with 90% iR compensation. **e** Nyquist plots in different electrolytes. **f** Tafel plots for corrosion potentials in real seawater. **g** The durability measurements of Fe-Ni_2P/$NiMoO_4$ at 1.0 A cm^{-2} constant current density in different electrolytes with 90% iR compensation. Source data are provided as a Source Data file.

between *OOH and adjacent hydrogen bonds[35]. Meanwhile, the stretching vibration of *OO in the characteristic intermediate from LOM can be observed at 1207 cm^{-1}, collectively demonstrating the compatible mechanism of both AEM and LOM in Fe-Ni_2P/$NiMoO_4$[35,36].

To distinguish in detail the contributions of each component in the Fe-Ni_2P/$NiMoO_4$ composite to the OER mechanism, chemical probes were employed to detect the forms and chemical properties of oxygenated intermediates on the catalyst surface. Methanol is known to compete for *OH intermediate adsorption on the catalyst surface under electrooxidation conditions. Consequently, methanol oxidation reaction (MOR) serves as a diagnostic measurement to evaluate *OH adsorption behavior, with MOR current density exhibiting a direct positive correlation with *OH surface coverage[37]. As depicted in Fig. 4d, Fe-Ni_2P/$NiMoO_4$ and $NiMoO_4$ exhibit significantly higher MOR current densities than Fe-Ni_2P at equivalent potentials, indicating more efficient and unimpeded *OH adsorption due to the introduction of O_V. Furthermore, the moderate enhancement of MOR current densities relative to the OER activity in Fe-Ni_2P/$NiMoO_4$ suggests that Fe species and O_V in the active phase jointly optimize the *OH adsorption energy and deprotonation kinetics in the AEM pathway. Similarly, tetramethylammonium cation (TMA^+) competitively adsorbs the characteristic intermediate (peroxide, O_2^{2-}) in the LOM pathway due to the strong electrostatic interaction, hindering the OER process dominated by LOM[11]. The negligible decrease of OER performance for $NiMoO_4$ in Fig. 4e suggests that R-$NiMoO_4$ primarily follows the AEM pathway. Conversely, Fe-Ni_2P/$NiMoO_4$ and Fe-Ni_2P exhibit marked deterioration in OER activity and kinetics, indicating that Fe doping induces the activation of oxygen ligands in active phases.

DFT calculation was employed to obtain a deeper understanding of the electron configuration and OER mechanisms (Supplementary Data 1). We constructed the theoretical structure models of the real active species for O_V-NiOOH, Ni(Fe)OOH, and O_V-Ni(Fe)OOH (Supplementary Fig. 49). As shown in Fig. 5a, the differential charge density analysis implies the covalent characteristic of Ni-O bonds in the foregoing three models, with the most discernible electron redistribution occurring between Ni and O atoms in O_V-Ni(Fe)OOH. Furthermore, the average Bader charge of surface Ni atoms progressively decreases from Ni(Fe)OOH (+1.259 |e|) to O_V-Ni(Fe)OOH (+1.233 |e|) and further to O_V-NiOOH (+1.228 |e|), suggesting the optimization of the electronic structure at Ni sites in O_V-Ni(Fe)OOH. Compared to Ni(Fe)OOH,

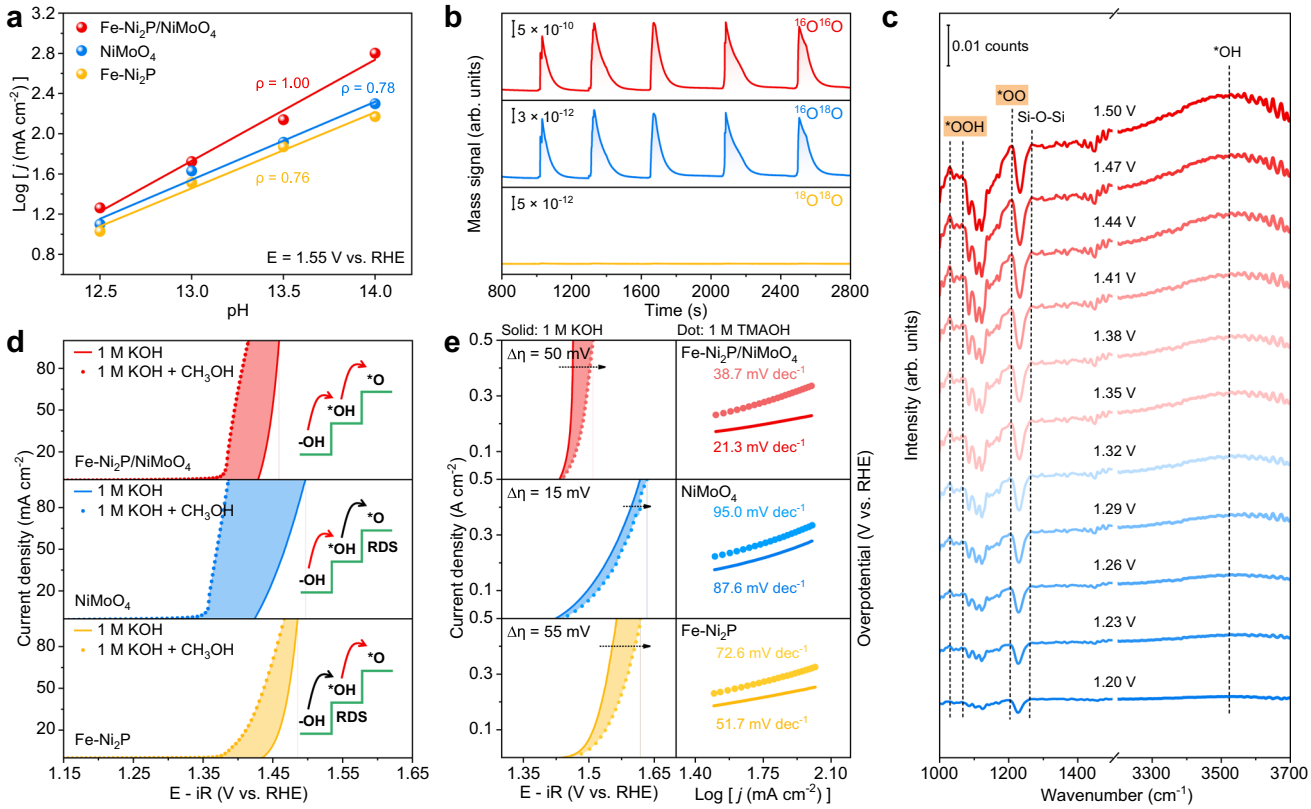

Fig. 4 | Dual-path OER mechanism experimental exploration. a The pH dependence of Fe-Ni_2P/$NiMoO_4$, $NiMoO_4$, and Fe-Ni_2P measured from the logarithm of current densities at 1.55 V vs. RHE in different concentrations of KOH solution and corresponding pH values (12.5, 13.0, 13.5, and 14.0). **b** In situ DEMS signals of Fe-Ni_2P/$NiMoO_4$ for $^{16}O^{16}O$, $^{16}O^{18}O$, and $^{18}O^{18}O$ related to testing time. **c** In situ ATR-SEIRAS collected from 1.20 to 1.50 V vs. RHE for Fe-Ni_2P/$NiMoO_4$. **d** LSV curves in 1 M KOH and 1 M KOH + CH_3OH with 90% iR compensation. **e** LSV curves measured in 1 M KOH and 1 M TMAOH, accompanied by the corresponding Tafel slopes with 90% iR compensation. Source data are provided as a Source Data file.

the Bader charge of Fe sites in O_V-Ni(Fe)OOH also slightly decreases, reflecting a lower valence state. Based on the analysis for density of states (DOS), the Ni 3*d* band center in O_V-Ni(Fe)OOH (-2.921 eV) shifts upward toward the Fermi level (E_F) with respect to Ni(Fe)OOH (−2.993 eV) and NiOOH (− 3.043 eV) (Fig. 5c). This result suggests that the Ni sites in OV-Ni(Fe)OOH show a tendency to donate electrons more readily, which may facilitate the adsorption of oxygen-containing intermediates, and could promote the AEM pathway in OER procedures. In addition, the higher orbital overlap of Ni 3*d* and O 2*p* suggests a stronger covalent hybridization between metal sites and oxygen ligands. Apparently, the rank of DOS overlap degree is Ni(Fe)OOH > O_V-Ni(Fe)OOH > NiOOH (as depicted in Fig. 5c). This observation, consistent with the XPS spectra (Fig. 2m), indicates the moderate Ni-O covalency in O_V-Ni(Fe)OOH under the co-modulation of Fe species and O_V, providing the prerequisite for triggering AEM-LOM dual-path.

The Gibbs free energy was computed to explore the optimal active sites for AEM and LOM in O_V-Ni(Fe)OOH (Supplementary Figs. 50–52). As shown in Fig. 5d, the deprotonation process (*OH → *O) at both Ni and Fe sites is identified as the rate-determining step (RDS), wherein the energy barrier at the Ni site is optimized to 2.20 eV. Considering the strong redox activity of Ni sites in O_V-Ni(Fe)OOH, Ni atoms may preferentially adsorb the OH^-, further coupling with oxygen ligands in the matrix after deprotonation, which follows the single-metal-site mechanism (SMSM), rather than the oxygen-vacancy-site mechanism (OVSM) (Supplementary Fig. 53). Consequently, we simulated the energy barriers of the LOM pathway under OVSM and SMSM. As presented in Fig. 5e, the RDS of the O site exhibits the optimal Gibbs free energy difference (ΔG) of 1.98 eV. In terms of kinetics, both Ni and Fe sites necessitate overcoming a large energy barrier from the initial state (IS) to transition state 1 (TS1) during the O-O coupling process, indicating a kinetically unfavorable behavior (Supplementary Fig. 54). These results suggest that O_V-Ni(Fe)OOH tends to follow the OVSM. Furthermore, comparing the theoretical overpotentials of AEM (0.97 V) and LOM (0.75 V) reveals that the AEM is inclined to occur at higher potentials. This may be beneficial for circumventing the structural collapse induced by the LOM pathway under high current densities, which potentially contribute to the development of OER catalyst together with activity and stability.

Based on the calculated PDOS at constant potential (U = 1.50 V vs. RHE), we investigated the alteration in the electronic configuration of electrocatalysts under operating conditions. As illustrated in Fig. 5g, the $\varepsilon_{Ni\text{-}3d}$ level in energy for O_V-Ni(Fe)OOH is slightly increased from −1.356 to −1.329 eV compared to Ni(Fe)OOH. The upward shift toward the E_F suggests the enhanced adsorption of oxygenated intermediates at Ni sites in O_V-Ni(Fe)OOH under 1.50 V. Conversely, the O 2*p* band center of O_V-Ni(Fe)OOH (−1.476 eV) can be observed with a downshifted $\varepsilon_{O\text{-}2p}$ value compared to Ni(Fe)OOH (−1.428 eV), which reduces the lattice oxygen activity, thereby suppressing the LOM pathway[38]. In addition, ab initio molecular dynamics (AIMD) simulations were also performed to evaluate the thermal stability of O_V-Ni(Fe)OOH. From Supplementary Fig. 55, the catalyst structure remains intact at 300 K after 5 ps. Even under practical operating conditions (T = 300 K, pH = 14, U = 1.50 V vs. RHE), the total energy fluctuates near the equilibrium value, with minor structural changes observed at the end of simulations (Fig. 5g), indicating the notable structural stability.

https://doi.org/10.1038/s41467-025-63844-x

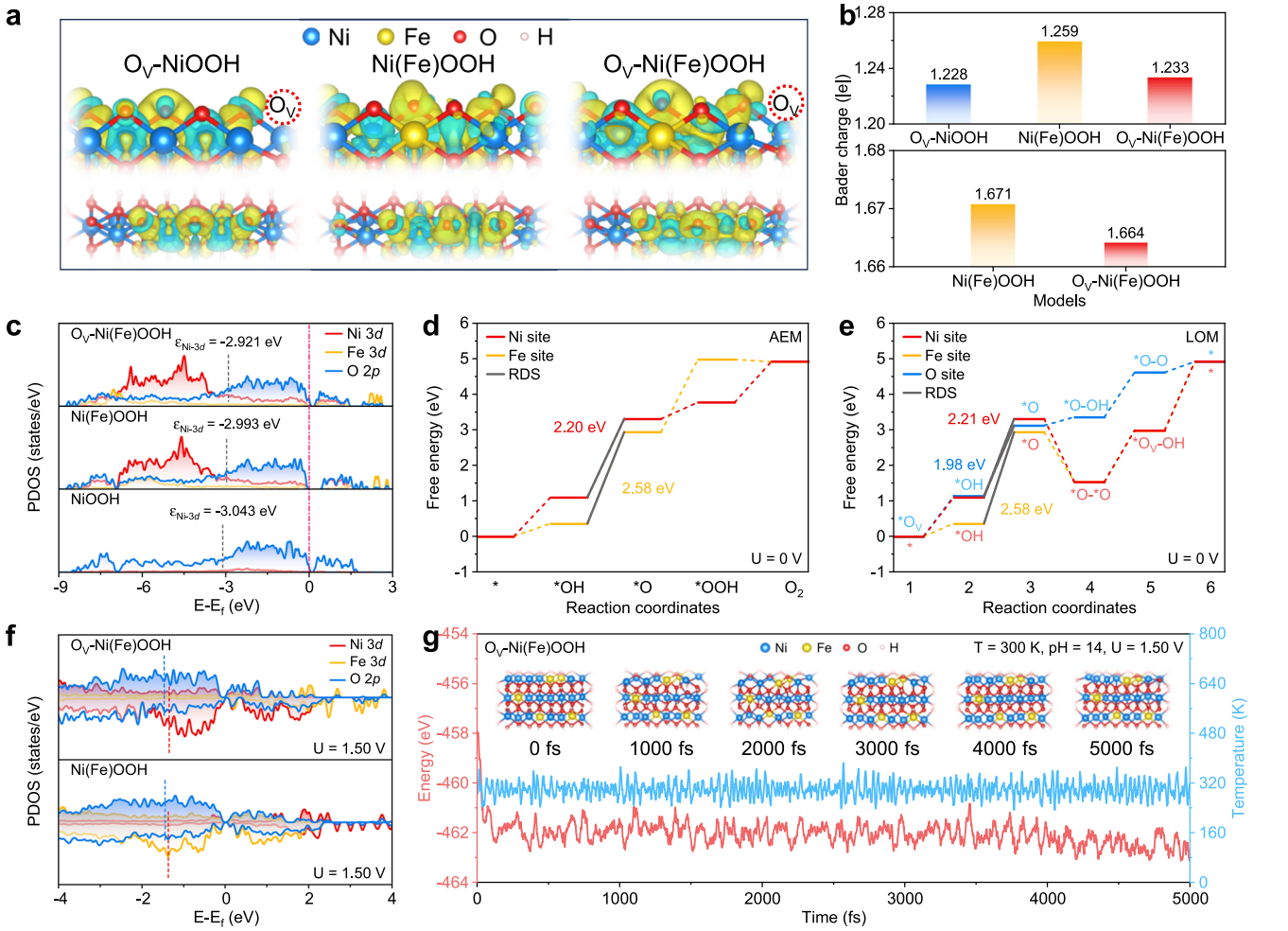

Fig. 5 | Dual-path OER mechanism computational exploration. a Differential charge density of O_V-NiOOH, Ni(Fe)OOH and O_V-Ni(Fe)OOH on the side and top view with an iso-surface value of 0.01 e Bohr^{-3} (yellow region: electron accumulation, cyan region: electron depletion). **b** The average Bader charge at metal sites on the outer surface of O_V-NiOOH, Ni(Fe)OOH and O_V-Ni(Fe)OOH. **c** Projected density of states (PDOS) for O_V-Ni(Fe)OOH, Ni(Fe)OOH, and NiOOH. The calculated OER free energy diagrams of the (**d**) AEM pathway, and (**e**) LOM pathway at different active sites in O_V-Ni(Fe)OOH. **f** Constant potential PDOS for O_V-Ni(Fe)OOH and Ni(Fe)OOH under 1.50 V vs. RHE. **g** Ab initio molecular dynamics (AIMD) simulation for O_V-Ni(Fe)OOH under OER conditions (T = 300 K, pH = 14, U = 1.50 V vs. RHE). Source data are provided as a Source Data file.

Freshwater/seawater splitting performance

Given the notable efficiency and durability of Fe-Ni_2P/$NiMoO_4$ for electrocatalytic freshwater/seawater oxidation, the activated Fe-Ni_2P/$NiMoO_4$ electrode was employed as the anode, while the as-prepared $MoNi_4$ HER catalyst served as the cathode, to construct an OWS electrolyzer for evaluating the application potential at industrial conditions. The $MoNi_4$ || Fe-Ni_2P/$NiMoO_4$ electrode-pair can reduce the cell voltages to 1.784 and 1.798 V in alkaline freshwater and seawater (Fig. 6a), respectively, which is competent to drive a current density of 1.0 A cm^{-2} at room temperature. It is noted that the OWS performance of $MoNi_4$ || Fe-Ni_2P/$NiMoO_4$ surpasses that of the benchmarked electrocatalyst pair (Pt/C || RuO_2), which requires 2.299 V (alkaline freshwater) and 2.413 V (alkaline seawater). Furthermore, after 100 h of continuous freshwater/seawater splitting at ampere-scale constant current density, the $MoNi_4$ || Fe-Ni_2P/$NiMoO_4$ system exhibits slight performance degradation, underscoring its notable durability. Moreover, as shown in Supplementary Fig. 56, a piece of solar cell sheet can drive OWS in the $MoNi_4$ || Fe-Ni_2P/$NiMoO_4$ system, featuring continuous bubble release of hydrogen and oxygen on the catalytic surface. This result validates the application potential of Fe-Ni_2P/$NiMoO_4$ in renewable energy conversion.

As shown in Fig. 6c and d, the anion exchange membrane (AEM) alkaline seawater electrolyzer using Fe-Ni_2P/$NiMoO_4$ and $MoNi_4$ electrocatalysts as anode and cathode, respectively, was assembled to simulate the industrial hydrogen production. The geometric area of both anode and cathode was 1 × 1 cm^2, and the exchange membrane was tailored to 2 × 2 cm^2. As illustrated in the j-V curves (Fig. 6e), the $MoNi_4$ || Fe-Ni_2P/$NiMoO_4$ electrolyzer exhibits superior AEM alkaline seawater splitting activity at room temperature, achieving a cell voltage of 2.182 V at 1.0 A cm^{-2}, surpassing the benchmarked Pt/C || RuO_2 pair (2.512 V at 1.0 A cm^{-2}). Notably, the $MoNi_4$ || Fe-Ni_2P/$NiMoO_4$ AEM system maintained stable seawater electrolysis for 500 h at the ampere-level current density (Fig. 6f), highlighting its long-term durability for industrial applications.

Discussion

To sum up, we designed Fe-Ni_2P decorated $NiMoO_4$ hydrate (Fe-Ni_2P/$NiMoO_4$) as a pre-catalyst with optimized electron configuration, thereby expediting the deep reconfiguration into O_V-Ni(Fe)OOH active phase. XPS and DFT analyses reveal that the Fe species and O_V synergistically regulate the electronic structure of NiOOH, providing proper covalency of Ni-O bonds for simultaneously triggering metal sites and oxygen ligands. In-situ ^{18}O isotope-labeling DEMS, in-situ ATR-SEIRAS, chemical probe experiments and DFT calculations confirm the AEM-LOM dual-path OER mechanism with optimized intermediates adsorption energy for O_V-Ni(Fe)OOH. Consequently, the activated

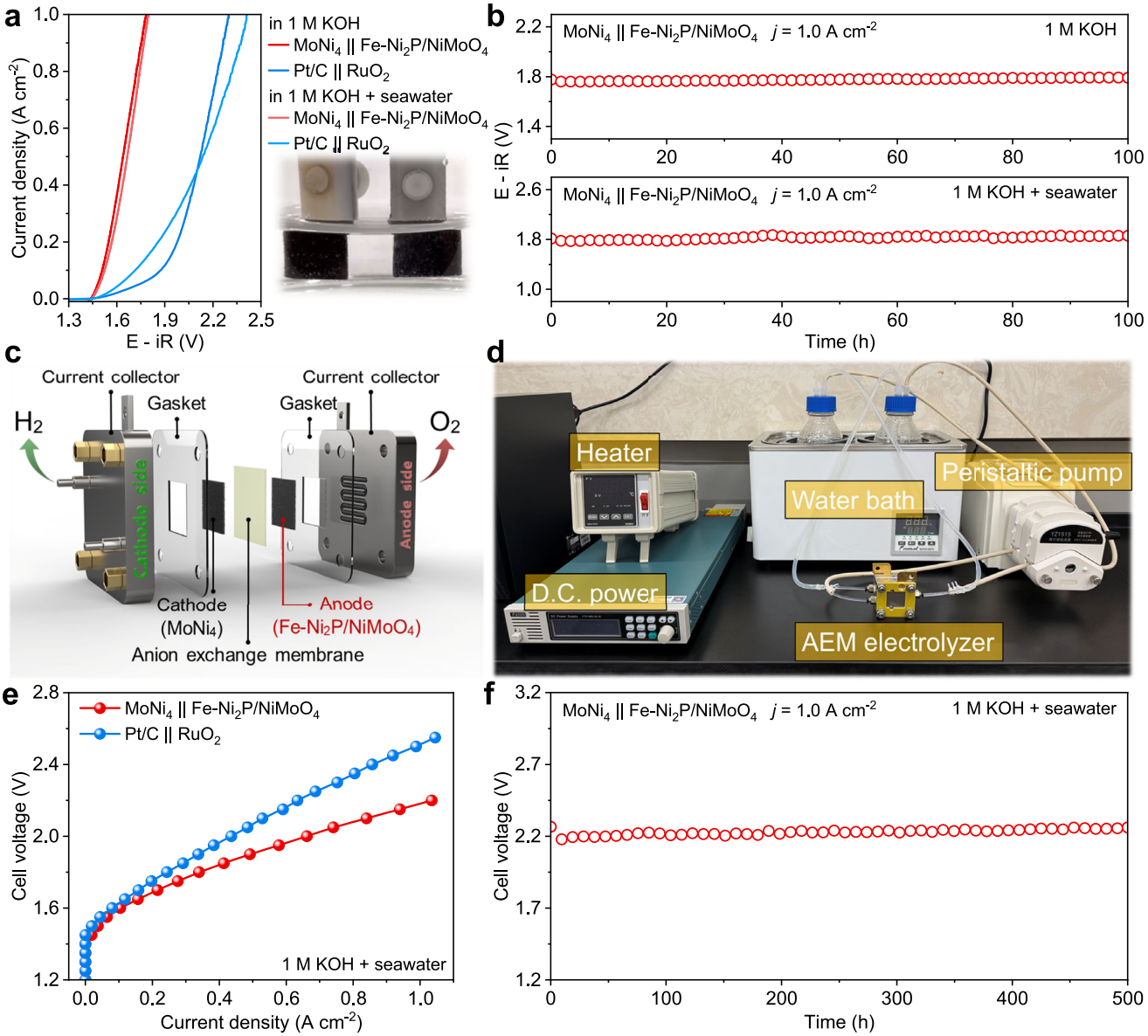

Fig. 6 | Water electrolyzer performance. a OWS LSV curves of $MoNi_4$ || Fe-Ni_2P/$NiMoO_4$ and Pt/C || RuO_2 with 90% iR-compensation. **b** The stability test of $MoNi_4$ || Fe-Ni_2P/$NiMoO_4$ at 1.0 A cm^{-2} with 90% iR-compensation. **c** Schematic diagram of AEMWE electrolyzer. **d** Optical photograph of the AEMWE system. **e** AEMWE *j*-V curves of $MoNi_4$ || Fe-Ni_2P/$NiMoO_4$ and Pt/C || RuO_2 in alkaline seawater without iR compensation. **f** The stability test at 1.0 A cm^{-2} for $MoNi_4$ || Fe-Ni_2P/$NiMoO_4$ based AEMWE system in alkaline seawater. Source data are provided as a Source Data file.

Fe-Ni_2P/$NiMoO_4$ catalyst demonstrates commendable OER activity. It features 274.5 ± 4.2 and 299.1 ± 2.8 mV overpotentials to drive the ampere-level freshwater and seawater oxidation, respectively, with negligible activity decay for 1000 and 500 h of continuous electrocatalysis in a three-electrode cell. Furthermore, the as-prepared Fe-Ni_2P/$NiMoO_4$ electrode, when employed as the anode in an AEMWE system, can achieve continuous ampere-level seawater electrolysis for 500 h at 1.0 A cm^{-2}.

Methods

Materials

Nickel nitrate hexahydrate ($Ni(NO_3)_2{\cdot}6H_2O$, 98%), potassium ferricyanide ($K_3Fe(CN)_6$, 99%), trisodium citrate ($C_6H_5Na_3O_7$, 99%), sodium hypophosphite ($NaH_2PO_2{\cdot}H_2O$, 95%), ammonium molybdate tetrahydrate ($(NH_4)_6Mo_7O_{24}$, 99%), ruthenium dioxide (RuO_2, 99.9%), carbon-supported platinum (Pt/C, 20 wt.%), potassium hydroxide (KOH, 98.5%), tetramethylammonium hydroxide (TMAOH) were sourced from Aladdin. Absolute ethanol, acetone, isopropanol, and hydrochloric acid were sourced from Zhisheng. All chemical reagents employed in this study were of purity exceeding analytical grade and utilized directly without undergoing any additional purification procedures. In the process of solution formulation, deionized (DI) water was exclusively used as the solvent to ensure consistent experimental conditions. We collected natural seawater from the Bohai Sea in Hebei Province, China, and used it after filtering.

Preparation of Fe-Ni_2P/$NiMoO_4$

Nikel foam (NF) was tailored to 3 × 4 cm^2 and rinsed by ultrasonication in acetone, diluted hydrochloric acid, absolute ethanol, and DI water, to eliminate the oils and oxides. To synthesis nickel molybdate hydrate ($NiMoO_4{\cdot}xH_2O$), $Ni(NO_3)_2{\cdot}6H_2O$ and $(NH_4)_6Mo_7O_{24}$ (molar ratio 4:1) with 60 mL of DI water were poured into the 100 mL Teflon-lined receptacle, and a homogeneous solution was obtained after continuous stirring for at least 15 min. Then, the receptacle was sealed into

a stainless-steel autoclave and kept at 150 °C for 6 h. Once cooled to room temperature, the product was repeatedly rinsed with DI water and absolute ethanol three times and dried in a vacuum oven at 60 °C for 12 h. Then, the as-prepared $NiMoO_4{\cdot}xH_2O$ was immersed in the 40 mL aqueous solution hybrid containing 20 mL solution A (0.8 mmol $Ni(NO_3)_2{\cdot}6H_2O$ and a certain dosage of $C_6H_5Na_3O_7$) and 20 mL solution B (0.5 mmol $K_3Fe(CN)_6$) for 26 h at room temperature to obtain PBA@$NiMoO_4$. Finally, a certain amount of $NaH_2PO_2{\cdot}H_2O$ was accurately weighed and put in an alumina ceramic container together with PBA@$NiMoO_4$. Placing the container in the central position of the quartz tube, wherein PBA@$NiMoO_4$ located at the downstream of the argon flow. We obtained the Fe-Ni_2P/$NiMoO_4$ after a 2 h low-temperature phosphorization process at 300 °C. The loading mass of Fe-Ni_2P/$NiMoO_4$ was determined by dividing the mass increase of the NF (before and after growth) by its geometric area (12 cm^2), yielding 10.0 ± 0.5 mg cm^{-2}.

Preparation of Fe-Ni_2P

The treated NF was directly immersed in the 40 mL mixed solution containing 0.8 mmol $Ni(NO_3)_2{\cdot}6H_2O$, 1.2 mmol $C_6H_5Na_3O_7$ and 0.5 mmol $K_3Fe(CN)_6$ to synthesize the NiFe PBA. The Fe-Ni_2P was obtained via the 2 h phosphorization process at 300 °C. The loading mass of Fe-Ni_2P is 10.0 ± 0.5 mg cm^{-2}.

Preparation of $MoNi_4$

The as-prepared $NiMoO_4{\cdot}xH_2O$ was heated at 400 °C for 2 h in a H_2/Ar (5:95) atmosphere to synthesize the $MoNi_4$ catalyst for HER. The loading mass of $MoNi_4$ is 10.0 ± 0.5 mg cm^{-2}.

Preparation of Pt/C and RuO_2 benchmarked catalysts

20 mg commercial Pt/C or RuO_2 powder was dispersed in a 2 mL mixture solution composed of 1.45 mL absolute ethanol, 0.5 mL isopropanol, and 0.05 mL Nafion solution. The homogeneous ink was obtained under ultrasonication for 2 h, and dropped upon two clean NF, respectively. Then, the Pt/C and RuO_2 catalysts loading on NF were prepared after drying in a vacuum oven at 60 °C for 12 h. The loading mass of benchmarked catalysts is 10.0 ± 0.5 mg cm^{-2}.

Material characterizations

The crystalline phase of all catalysts was measured via powder XRD using a D/Max-2500/PC X-ray diffractometer with Cu Kα radiation (λ = 1.5418 Å) over an angle (2θ) range from 5 to 80 degree under the scanning rate of 5 °/min. Raman spectra were recorded on a Renishaw inVia laser Raman spectrometer with a laser excitation of 532 nm. An XPS test was performed on the ESCALab MKII X-ray photoelectron spectrometer equipped with Al Kα X-ray radiation as the excitation source. The morphology and microstructure of the samples were characterized via field-emission scanning electron microscopy (FESEM, Zeiss SUPRA 55), transmission electron microscopy (TEM, Hitachi-7700), high-resolution transmission electron microscopy (HRTEM, FEI TALOS F200) combined with high-angle annular darkfield-scanning transmission electron microscopy (HAADF-STEM) and energy-dispersive X-ray spectroscopy (EDS). The accurate element contents in the catalysts was obtained through the inductively coupled plasma-mass spectrometry (ICP-MS, PerkinElmer NexION 300X).

Electrochemical measurements

Unless specified, all electrochemical measurements were performed on the Corrtest CS310MA electrochemical workstation (Wuhan Corrtest Instruments Corp., Ltd.) at room temperature. Electrolytes were freshly prepared before each test to avoid storage-related changes: 1 M KOH (28.5 g KOH in 500 mL DI water, pH = 13.82 ± 0.04), 1 M KOH + 0.5 M NaCl (28.5 g KOH and 14.6 g NaCl in 500 mL DI water, pH = 13.80 ± 0.05), and 1 M KOH + seawater (28.5 g KOH in 500 mL seawater, pH = 13.69 ± 0.03). Three-electrode system was assembled in a borosilicate glass cell (Tianjin Gaoss Union C002, 50 mL) with the electrolyte volume of 40 mL. The as-prepared catalysts were directly applied as the working electrode with 1 × 1 cm^2 immersing area in the electrolyte. A standard Hg/HgO electrode (1 M KOH) and a graphite rod (purity: 99%) were used as the reference electrode and the counter electrode, respectively. Before all electrochemical measurements, the Hg/HgO reference electrode was calibrated using a three-electrode system, with two clean Pt foils serving as the counter electrode and working electrode, respectively. Prior to calibration, high-purity H_2 was continuously introduced into the electrolyte for one hour to saturate the solution with hydrogen. Then, cyclic voltammetry (CV) curves were recorded with a scan rate of 2 mV s^{-1} at room temperature, as shown in Supplementary Fig. 19.

Linear sweep voltammetry (LSV) was operated under a scanning rate of 5 mV s^{-1}. All the potentials in LSV were iR-compensated (compensation level: 90%), and the resistance (R_s) for iR-compensation was tested at the open circuit potential (OCP), measured to be 0.60 ± 0.01 Ω and 0.75 ± 0.05 Ω in alkaline freshwater and seawater, respectively. Mean values ± S.D. were obtained by three independent measurements. The in-situ electrochemical impedance spectroscopy (EIS) was operated from 100 kHz to 0.01 Hz at a serious voltage with a small amplitude (30 mV). The durability tests were performed by chronopotentiometry (CP) at the current density of 1.0 A cm^{-2}. Cyclic voltammetry (CV) was operated at the potential range of 0.30 to 0.40 V vs. Hg/HgO with a series scanning rate of 20, 40, 60, 80, and 100 mV s^{-1}. The electric double-layer capacitance (C_{dl}) was calculated by the current density difference (Δj/2) in the center of the potential range under different scanning rates. ECSA was established by the following equation:

$$ECSA = C_{dl}/C_s \times A \tag{1}$$

Where the specific capacity C_s is 0.04 mF cm^{-2} in 1 M KOH electrolyte, and A is the geometric area of working electrode soaking in the electrolyte (1 × 1 cm^2).

All measured potentials vs. Hg/HgO were converted to reversible hydrogen electrode (RHE) by the Nernst equation in addition to special note:

$$E\,(V\ vs.RHE) = E\,(V\ vs.Hg/HgO) + 0.098 + 0.0592 \times pH \tag{2}$$

Overall water splitting (OWS) measurements were tested under a two-electrode system. The as-synthesized Fe-Ni_2P/$NiMoO_4$ was used as the anode for OER, while the $MoNi_4$ served as the cathode for HER. For the performance comparison, the as-prepared commercial Pt/C and RuO_2 catalysts were employed as cathode for HER and anode for OER, respectively. LSV curves of OWS were measured in 1 M KOH, 1 M KOH + 0.5 M NaCl, and 1 M KOH + seawater electrolyte at a sweeping rate of 5 mV s^{-1} with 90% iR-compensation. The durability of the catalyst was tested via chronopotentiometry (CP) at a constant current density of 1.0 A cm^{-2}.

In situ Raman measurements

The in-situ Raman spectra were collected by a Renishaw inVia laser Raman spectrometer with a laser excitation of 532 nm. The as-prepared catalysts were used as the work electrodes, with an Ag/AgCl and a graphite rod as the reference and counter electrodes, respectively. The N_2-saturated 0.1 M KOH was employed as the electrolyte to slow down the gas bubble production under OER potentials. The Raman spectra were obtained on the multi-potential steps test, which was conducted on a CHI 760E electrochemical workstation (Shanghai Chenhua Instrument Co., Ltd), with the potential windows from 1.20 to 1.50 V vs. RHE.

In situ isotope-labeled DEMS measurements

Isotope-labeled DEMS measurements were performed on a QAS 100 device (Linglu Instruments, Shanghai). The $H_2{}^{18}O$ (^{18}O abundance: 98%) was purchased from Beijing InnoChem Science & Technology Co., Ltd. The porous polytetrafluoroethylene (PTFE) membrane supported catalysts were used as the working electrode, with an Hg/HgO and a graphite rod as the reference and counter electrodes, respectively. The PTFE membrane (pore size ≤ 20 nm, porosity ≥ 50%) was provided by Linglu Instruments. Firstly, the samples were labeled with ^{18}O-isotopes by the LSV activation for six times in the 0.2 - 0.8 V vs. Hg/HgO potential window in 1 M KOH solution with $H_2{}^{18}O$ (scan rate: 5 mV s^{-1}). Subsequently, the ^{18}O-isotope labeled samples were carefully rinsed with $H_2{}^{16}O$ several times to remove the residual $H_2{}^{18}O$. Finally, LSV tests were performed for the labeled catalysts in 1 M KOH with $H_2{}^{16}O$ from 0.2 to 0.8 V vs. Hg/HgO, and the produced oxygen with different molecular weights during OER was detected in real time by mass spectroscopy.

In situ ATR-SEIRAS measurements

The surface-enhanced infrared absorption spectroscopy (SEIRAS) with attenuated total reflection (ATR) was employed to detect the intermediates of the OER process. The electrochemical ATR-SEIRAS measurements were used on the Thermo Nicolet 8700 spectrometer equipped with the mercury-cadmium-telluride detector cooled by liquid nitrogen. Utilizing the two-step wet chemical method, Au thin film (~ 60 nm) was deposited on the surface of the Si prism for IR reflection enhancement. Before the chemical deposition of Au, the Si prism was polished with Al_2O_3 and SiO_2 suspension, respectively, and cleaned in DI water with ultrasonication. Then the Si prism was immersed in a mixed solution of 98% H_2SO_4 and 30% H_2O_2 (volumetric ratio = 7:3) for 30 min. After rinsing off the residual acid solution with DI water, the Si prism was soaked in the quartz crucible containing 40% NH_4F aqueous solution and Au plating bath for 3 min, respectively, to prepare Au film on the IR reflection surface. 10 mg catalyst powder was dispersed in the 1 mL mixture solution comprised of 975 μL DI water and isopropanol (volumetric ratio = 1:1), and 25 μL Nafion solution under ultrasonication for 2 h to obtain catalyst ink. 30 μL ink was dropped and dried on the Au-coated prism as the working electrode. The saturated Ag/AgCl electrode (reference electrode) and Pt foil (counter electrode, $1 \times 1\,cm^2$) were assembled into a spectro-electrochemical cell with the Au-film prism. The N_2-saturated 0.1 M KOH was employed as the electrolyte to slow down the gas bubble production under OER potentials. The electrochemical ATR-SEIRAS was obtained on the multi-potential steps test, which was conducted on a CHI 760E electrochemical workstation (Shanghai Chenhua Instrument Co., Ltd), with the open circuit potential and potential windows from 1.20 to 1.50 V vs. RHE. The spectral resolution was 4 cm^{-1} for all the measurements. The spectra were obtained via the built-in processing program by equation:

$$A = -\log(R_{Es}/R_{ER}) \tag{3}$$

Where A is absorbance, R_{Es} is reflection under potentials range, and R_{ER} is reflection at open circuit potential.

AEMWE measurements

Anion exchange membrane (AEM) water electrolyzers were employed to evaluate the practical performance of electrocatalysts. In detail, the bipolar plates with serpentine flow channel (effective area: $1 \times 1\,cm^2$) were served as the current collectors, and gaskets (thickness: 0.8 mm) were used to secure the anion exchange membrane. Commercial Ni foam (thickness: 1 mm) simultaneously functioned as the gas diffusion layer (GDL) and catalyst support for the cathode and anode. Commercial PiperION-A (thickness: 40 μm, size: $2 \times 2\,cm^2$) membrane was employed as the AEM, and was pretreated by immersion in the 1 M KOH solution at room temperature for 2 h before utilization. The membrane was then sandwiched between the cathode and anode to form the membrane electrode assembly (MEA). Finally, the MEA was assembled with gaskets and current collectors, and clamped under a torque of 3.0 N m to ensure equal compression.

The AEMWE performance was evaluated using an FTP1060 D.C. power supply (Shenzhen Faithtech Co., Ltd.) at room temperature. Specifically, the *j*-V polarization curves were determined via the constant-voltage method, with each point recorded once the current had stabilized. During this process, a peristaltic pump was operated to supply the 1 M KOH + seawater solution at a flow rate of 40 mL min^{-1}. The long-term stability measurements were performed at a constant current of 1.0 A with a flow rate of 40 mL min^{-1}.

DFT calculations

In Density Functional Theory (DFT) calculations, structural optimizations were performed under the scheme of generalized gradient approximation (GGA) using the Perdew-Burke-Ernzerhof (PBE) functional[39], as embedded in the Vienna Ab-initio Simulation Package (VASP)[40,41]. The projector augmented-wave (PAW) method was employed to treat interactions between ion cores and valence electrons[42,43]. The plane-wave cutoff energy was fixed to 450 eV. The Van der Waals interactions were considered by grime's DFT-D3 method[44,45]. The self-consistent calculations applied a convergence energy threshold of 10^{-5} eV. The equilibrium geometries and lattice constants were optimized with maximum stress on each atom within 0.02 eV $Å^{-1}$. During the relaxation, the Brillouin zone with a $3 \times 2 \times 1$ Gamma-centered grid was used. The Climbing Image Nudged Elastic Band (CI-NEB) method has been used to investigate the energy barrier of O-O coupling processes. Spin-polarized calculations were performed for this calculation.

For each elementary step, the Gibbs reaction free energy ΔG is defined as the difference between free energies of the initial and final states and is given by the expression:

$$\Delta G = \Delta E + \Delta E_{ZPE} - T\Delta S \tag{4}$$

where ΔE is the reaction energy of reactant and product molecules adsorbed on catalyst surface, obtained from DFT calculations; ΔE_{ZPE} and ΔS are the change in zero-point energies and entropy due to the reaction.

The ab initio molecular dynamics (AIMD) for 5 ps is performed within the canonical (NVT) ensemble by Nosé-Hoover thermostats with a time step of 1.0 fs at a finite temperature of 300 K. In order to explicitly embody the electrochemical conditions in the model that are closer to reality in the model, we implemented the potentiostatic simulation by using CP-VASP, the chosen electrochemical conditions are pH = 14 and U = 1.50 V vs. RHE. CP-VASP software can easily control the surface electrode potential by removing or adding charges from the system to obtain the grand canonical energy (GCE). The specific implementation method can be referred to in the reported literature[46]. According to the calculation method mentioned in this paper, the absolute electrode potential of the standard hydrogen electrode (SHE) is − 4.15 V.

Data availability

The source data generated in this study are provided in the Source Data file. Source data are provided in this paper.

References

1. Huang, W. et al. Ligand modulation of active sites to promote electrocatalytic oxygen evolution. *Adv. Mater.* **34**, 2200270 (2022).
2. Cai, Z. et al. Reinforced layered double hydroxide oxygen-evolution electrocatalysts: a polyoxometallic acid wet-etching approach and synergistic mechanism. *Adv. Mater.* **34**, 2110696 (2022).

3. Wang, T. et al. NiFe (Oxy) hydroxides derived from NiFe disulfides as an efficient oxygen evolution catalyst for rechargeable Zn-air batteries: the effect of surface S residues. *Adv. Mater.* **30**, 1800757 (2018).
4. Chen, L. et al. Seawater electrolysis for fuels and chemicals production: fundamentals, achievements, and perspectives. *Chem. Soc. Rev.* **53**, 7455–7488 (2024).
5. Liang, J. et al. Efficient bubble/precipitate traffic enables stable seawater reduction electrocatalysis at industrial-level current densities. *Nat. Commun.* **15**, 2950 (2024).
6. Liu, W. et al. Self-protecting CoFeAl-layered double hydroxides enable stable and efficient brine oxidation at 2 A cm^{-2}. *Nat. Commun.* **15**, 4712 (2024).
7. Liang, J. et al. Expanded negative electrostatic network-assisted seawater oxidation and high-salinity seawater reutilization. *ACS Nano* **19**, 1530–1546 (2025).
8. Wang, A. et al. Enhancing oxygen evolution reaction by simultaneously triggering metal and lattice oxygen redox pair in iridium loading on Ni-doped Co_3O_4. *Adv. Energy Mater.* **13**, 2302537 (2023).
9. Dionigi, F. et al. In-situ structure and catalytic mechanism of NiFe and CoFe layered double hydroxides during oxygen evolution. *Nat. Commun.* **11**, 2522 (2020).
10. Song, J. et al. A review on fundamentals for designing oxygen evolution electrocatalysts. *Chem. Soc. Rev.* **49**, 2196–2214 (2020).
11. Huang, Z. et al. Tuning of lattice oxygen reactivity and scaling relation to construct better oxygen evolution electrocatalyst. *Nat. Commun.* **12**, 3992 (2021).
12. Xie, X. et al. Oxygen evolution reaction in alkaline environment: material challenges and solutions. *Adv. Funct. Mater.* **32**, 2110036 (2022).
13. Zhang, G. et al. Selective activation of lattice oxygen site through coordination engineering to boost the activity and stability of oxygen evolution reaction. *Angew. Chem. Int. Ed.* **63**, e202407509 (2024).
14. Lin, C. et al. In-situ reconstructed Ru atom array on α-MnO_2 with enhanced performance for acidic water oxidation. *Nat. Catal.* **4**, 1012–1023 (2021).
15. Wang, Z., Goddard III, W. A. & Xiao, H. Potential-dependent transition of reaction mechanisms for oxygen evolution on layered double hydroxides. *Nat. Commun.* **14**, 4228 (2023).
16. Xin, S. et al. Coupling adsorbed evolution and lattice oxygen mechanism in Fe-$Co(OH)_2$/Fe_2O_3 heterostructure for enhanced electrochemical water oxidation. *Adv. Funct. Mater.* **33**, 2305243 (2023).
17. Liu, X. et al. Complete reconstruction of hydrate pre-catalysts for ultrastable water electrolysis in industrial-concentration alkali media. *Cell Rep. Phys. Sci.* **1**, 100241 (2020).
18. Dürr, R. N. et al. From $NiMoO_4$ to γ-NiOOH: detecting the active catalyst phase by time resolved in situ and operando Raman spectroscopy. *ACS Nano* **15**, 13504–13515 (2021).
19. Li, J. et al. Low-crystalline bimetallic metal-organic framework electrocatalysts with rich active sites for oxygen evolution. *ACS Energy Lett.* **4**, 285–292 (2018).
20. Huang, Y., Wang, Z., Xiao, H., Liu, Q. & Wang, X. Activating and stabilizing lattice oxygen via self-adaptive Zn-NiOOH sub-nanowires for oxygen evolution reaction. *J. Am. Chem. Soc.* **146**, 29006–29016 (2024).
21. Zhang, Y. et al. Activating lattice oxygen based on energy band engineering in oxides for industrial water/saline oxidation. *Energy Environ. Sci.* **17**, 3347–3357 (2024).
22. Fan, W. et al. Biomimetic Stylophora pistillata-like $NiMoO_4$/NiFeS crystalline-amorphous phase boundary activated lattice oxygen mechanism for efficient electrochemical water oxidation. *Chem. Eng. J.* **502**, 158106 (2024).
23. Zhu, J., Qian, J., Peng, X., Xia, B. & Gao, D. Etching-induced surface reconstruction of $NiMoO_4$ for oxygen evolution reaction. *Nano Micro Lett.* **15**, 30 (2023).
24. Jiang, R. et al. Redox promoted rapid and deep reconstruction of defect-rich nickel precatalysts for efficient water oxidation. *Small* **20**, 2401384 (2024).
25. Lyons, M. E., Doyle, R. L. & Brandon, M. P. Redox switching and oxygen evolution at oxidized metal and metal oxide electrodes: iron in base. *Phys. Chem. Chem. Phys.* **13**, 21530–21551 (2011).
26. Zhu, K., Zhu, X. & Yang, W. Application of in situ techniques for the characterization of NiFe-based oxygen evolution reaction (OER) electrocatalysts. *Angew. Chem. Int. Ed.* **58**, 1252–1265 (2019).
27. Huang, J. et al. Identification of key reversible intermediates in self-reconstructed nickel-based hybrid electrocatalysts for oxygen evolution. *Angew. Chem. Int. Ed.* **131**, 17619–17625 (2019).
28. Ye, P. et al. Lattice oxygen activation and local electric field enhancement by co-doping Fe and F in CoO nanoneedle arrays for industrial electrocatalytic water oxidation. *Nat. Commun.* **15**, 1012 (2024).
29. Wang, H. et al. Application progress of $NiMoO_4$ electrocatalyst in basic oxygen evolution reaction. *Catal. Sci. Technol.* **14**, 533–554 (2024).
30. Guan Xu, H. et al. Oxygen plasma triggered Co-O-Fe motif in Prussian blue analogue for efficient and robust alkaline water oxidation. *Angew. Chem. Int. Ed.* **64**, e202415423 (2025).
31. Zhou, L. et al. A restricted dynamic surface self-reconstruction toward high-performance of direct seawater oxidation. *Nat. Commun.* **15**, 2481 (2024).
32. Song, Y. et al. Coupled amorphous NiFeP/cystalline Ni_3S_2 nanosheets enables accelerated reaction kinetics for high current density seawater electrolysis. *Appl. Catal. B Environ.* **352**, 124028 (2024).
33. Mefford, J. T. et al. Water electrolysis on $La_{1-x}Sr_xCoO_{3-\delta}$ perovskite electrocatalysts. *Nat. Commun.* **7**, 11053 (2016).
34. Liu, L. et al. Antagonism effect of residual S triggers the dual-path mechanism for water oxidation. *J. Energy Chem.* **93**, 568–579 (2024).
35. Sivasankar, N., Weare, W. W. & Frei, H. Direct observation of a hydroperoxide surface intermediate upon visible light-driven water oxidation at an Ir oxide nanocluster catalyst by rapid-scan FT-IR spectroscopy. *J. Am. Chem. Soc.* **133**, 12976–12979 (2011).
36. Hao, Y. et al. Switching the oxygen evolution mechanism on atomically dispersed Ru for enhanced acidic reaction kinetics. *J. Am. Chem. Soc.* **145**, 23659–23669 (2023).
37. Mei, Y. et al. High-entropy alloy with Mo-coordination as efficient electrocatalyst for oxygen evolution reaction. *ACS Catal.* **12**, 10808–10817 (2022).
38. Wu, T. et al. Iron-facilitated dynamic active-site generation on spinel $CoAl_2O_4$ with self-termination of surface reconstruction for water oxidation. *Nat. Catal.* **2**, 763–772 (2019).
39. Perdew, J. P., Burke, K. & Ernzerhof, M. Generalized gradient approximation made simple. *Phys. Rev. Lett.* **77**, 3865–3868 (1996).
40. Kohn, W. & Sham, L. J. Self-consistent equations including exchange and correlation effects. *Phys. Rev.* **140**, A1133–A1138 (1965).
41. Raybaud, P., Hafner, J., Kresse, G., Kasztelan, S. & Toulhoat, H. Ab initio study of the H_2-H_2S/MoS_2 gas-solid interface: The nature of the catalytically active sites. *J. Catal.* **189**, 129–146 (2000).
42. Kresse, G. & Joubert, D. From ultrasoft pseudopotentials to the projector augmented-wave method. *Phys. Rev. B.* **59**, 1758–1775 (1999).
43. Blöchl, P. E. Projector augmented-wave method. *Phys. Rev. B.* **50**, 17953–17979 (1994).
44. Grimme, S., Antony, J., Ehrlich, S. & Krieg, H. A consistent and accurate ab initio parametrization of density functional dispersion

correction (DFT-D) for the 94 elements H-Pu. *J. Chem. Phys.* **132**, 154104 (2010).
45. Grimme, S., Ehrlich, S. & Goerigk, L. Effect of the damping function in dispersion corrected density functional theory. *J. Comput. Chem.* **32**, 1456–1465 (2011).
46. Zhao, X. & Liu, Y. Origin of selective production of hydrogen peroxide by electrochemical oxygen reduction. *J. Am. Chem. Soc.* **143**, 9423–9428 (2021).

Acknowledgements

The authors acknowledge the financial support from the National Natural Science Foundation of China (Grant No. 22379112, 21671168) and the financial support from the Natural Science Foundation of Hebei Province (Grant No. B2021203016, 22281403Z), S&T Program of Hebei (236Z4405G) and Hebei Youth Top-notch Talent Support Program. The authors thank the subsidy for Hebei Key Laboratory of Applied Chemistry after Operation Performance (22567616H).

Author contributions

X.T. conducted most experiments and data analysis. X.W. and J.J. helped with HAADF-STEM and TEM measurements. H.L. assisted in electrochemical measurements. L.H. and F.G. oversaw the project and assisted in data analysis. The final version of the text has been carefully reviewed and approved by all authors for submission.

Competing interests

All authors declare no competing interests.

Additional information

Supplementary information The online version contains supplementary material available at https://doi.org/10.1038/s41467-025-63844-x.

Correspondence and requests for materials should be addressed to Li Hou or Faming Gao.

Peer review information *Nature Communications* thanks Jungang Hou, Subrata Kundu and the other anonymous reviewer(s) for their contribution to the peer review of this work. A peer review file is available.